

Remote sensing of brine shrimp cysts in salt lakes

Lin Qi¹, Yao Yao¹, David E. English¹, Ronghua Ma², John Luft³, and Chuanmin Hu^{1*}

¹College of Marine Science, University of South Florida, St. Petersburg, Florida, USA

²State Key Laboratory of Lake Science and Environment, Nanjing Institute of Geography and Limnology, Chinese Academy of Sciences, 73 East Beijing Road, Nanjing 210008, China

³Utah Division of Wildlife Resources, 4790 South 7500 West, Hooper, Utah, USA

*Correspondence to: huc@usf.edu

Abstract

Using laboratory and field experiments as well as spectral analysis of satellite images, we demonstrate that surface aggregations of brine shrimp (*Artemia*) cysts (BSC) in salt lakes can be identified unambiguously in satellite imagery. This is because of the unique reflectance spectral shapes of the BSC image slicks, where a sharp and monotonic increase in reflectance is found at wavelengths > 550 nm and two inflection points are found around ~550 nm and ~650 nm. Such spectral characteristics differentiate BSC slicks from other floating matters. Based on this principle, a deep learning model is developed to extract BSC features from MERIS (Medium Resolution Imaging Spectrometer, 2002 - 2012) and OLCI (Ocean and Land Colour Instrument, 2016 - present) satellite images to quantify BSC abundance, spatial distribution patterns, and their temporal changes in the Great Salt Lake (GSL), the world's largest contributor of BSC commercial products. A clear seasonality is found in BSC abundance, with the primary peak in April – May and secondary peak in October – November. The two peaks may be explained by food availability to brine shrimp. The inter-annual variability and the recent increasing trend in BSC abundance, on the other hand, are difficult to explain by fluctuations in wind, temperature, or salinity, while recent increase in commercial harvest does not appear to be associated with the variability in BSC abundance estimated by satellites. Because many salt lakes around the world, for example the Aral Sea, Lake Urmia, and the Dead Sea, also show BSC slicks in satellite imagery, this study suggests that it is possible to perform a systematic evaluation of BSC abundance and possibly brine shrimp populations in all major salt lakes, especially under a changing climate and increased human activities.

Keywords: brine shrimp (*Artemia*), brine shrimp cysts (BSC), Great Salt Lake (GSL), Aral Sea, Lake Urmia, Dead Sea, remote sensing, MERIS, OLCI, Spectral Angle Mapper, similarity index

1. Introduction

In many inland salt lakes, coastal lagoons, and solar saltworks throughout the world, especially in hypersaline waters where few fish can survive (Vanhaecke et al., 1987; Van Stappen, 1996), brine shrimp play an important role in the salt water ecosystem as they feed on algae and feed birds and other beetles (Belovsky & Perschon 2019; Belovsky et al. 2011). There are many types of birds that need to feed on large numbers of brine shrimp and eggs to continue their long-distance migrations (Roberts & Conover, 2013).

Brine shrimp usually survive in waters with salinity between ~30 – 300g/L and water temperature between 6- 35°C (Hammer 1978; Van Stappen, 1996). Female shrimp can produce eggs, called cysts, which can float and aggregate into large masses as streaks of meters in width and hundreds of meters in length on the water surface. While Adult brine shrimp tend to die at low temperatures (below ~6°C), their cysts can survive such winter temperatures and recovery quickly under the right temperature and salinity conditions (Vanhaecke et al., 1987; Van Stappen, 1996; Wurtsbaugh & Maciej Gliwicz, 2001). Because of their durability, brine shrimp cysts (BSC) can be harvested, processed, stored, and commercialized, which can serve as live food source for aquaculture as the dried BSC can be hatched under appropriate conditions. The Great Salt Lake (GSL), located in Utah, USA, is a major source of BSC products in the world (Belovsky & Perschon, 2019). Commercial harvest of BSC in the GSL started from the 1950s, with annual BSC production of several million pounds, supporting a multi-million-dollar industry. Assessment of the BSC distributions and their long-term and short-term changes can provide useful information to assist in management decisions, for example to help determine where, when, and how much can be harvested. Traditionally, this is done by field or airborne surveys (Sura & Belovsky, 2016). However, such surveys are typically limited in both spatial and temporal coverage. On the other hand, although satellite remote sensing can provide more synoptic and temporal coverage, to date, satellite remote sensing in fisheries studies is mainly used to assess the water environment (e.g., temperature, salinity, chlorophyll concentration,

water turbidity, etc). A literature review shows nearly no satellite-based remote sensing detection of BSC, let alone detection of brine shrimp in salt lakes.

One exception is shown in Qi et al. (2020), who speculated that some of the “slicks” in satellite images collected over the GSL could be caused by aggregations of BSC. This is because BSC are known to be able to float and aggregate on the water surface, and the image slicks show spectral shapes different from other floating matters. However, direct validation from laboratory or field measurement is still lacking. In the satellite images, there are also other image slicks that show different spectral shapes, and they are speculated to be caused by white foams. Consequently, whether or not it is possible to detect and quantify BSC in the GSL or other salt lakes still remains a challenge to be addressed.

The objective of this study is to address such a challenge, specifically: 1) to determine spectral characteristics of BSC and demonstrate the remote sensing feasibility; 2) to develop a robust algorithm to delineate BSC features in satellite images; 3) to quantify the relative abundance of BSC in the GSL from satellite images; 4) to study the seasonal and inter-annual changes of BSC in the GSL. We achieve these objectives through laboratory and field measurements, development of a deep-learning algorithm, and time-series analysis of multi-sensor satellite data. Furthermore, we hope this study will promote research to perform a systematic evaluation of long-term changes of BSC in other salt-water lakes worldwide.

2. Data and methods

2.1. Study area

The GSL is a remnant of the historic Bonneville Lake, with an area of about 4,400km² and a maximum depth of 10 m. It is now the fourth largest salt lake in the world and the largest in the North American continent. In 1959, a rock-filled railroad was built by Union Pacific Railroad to divide the GSL into two sections. This division caused the two parts of lake to be ecologically different, with the north arm having a high salinity of ~300 g/L and the south arm having a lower salinity of ~140g/L due to freshwater inflow from the watershed (White et al., 2014). Differences in salinity also lead to different microorganisms, ecologies, and even the water

color in the two arms (Baxter 2018; Baxter & Butler, 2020). The north arm is mainly dominated by the archaea (single-celled prokaryotes, commonly found in highly saline waters) that can make the lake water appear pink, while the south arm appears green with abundant *Dunaliella* (one type of halophile green micro-algae), a major food source to brine shrimp (Baxter & Butler, 2020; Stephens & Gillespie, 1976; Wurtsbaugh & Maciej Gliwicz, 2001). According to the reports of the Utah Division of Wildlife Resources (UDWR), although brine shrimp can be found occasionally in the north arm, most BSC harvest activities are concentrated in the south arm. Therefore, this study is focused on the south arm.

2.2. Laboratory experiment

To determine the optical signature that BSC aggregations may contribute to the spectral reflectance estimated from satellite imagery, the spectral reflectance of commercial BSC particles was measured in the laboratory. Such measured BSC reflectance was expected to provide a spectral shape similar to BSC reflectance spectral shape measured in the field or estimated from satellite imagery, as shown below. The BSC sample was purchased online, with the product called “Noa Store Brine Shrimp Eggs Artemia Cysts 90 Percent Hatch Rate Fish Food” and the product labeled “These GSL cysts are over-wintered, washed, dried, and tested under strict guidelines before categorizing into the different hatch rate categories.”

Measured amounts of dry BSC particles were added to shallow, transparent, 8.5-cm diameter containers filled with hypersaline water (salinity ~ 140 g/L, similar to GSL salinity) so that the BSC coverage of the water’s surface varied from partial to nearly complete (Fig. 1a). The BSC particles floated on the water for >24 hours to allow partial rehydration. To estimate the floating BSC reflectance, each BSC container was transferred to a larger black container containing ~ 40 -cm deep hypersaline water to reduce possible bottom interference (Fig. 1a). Most of the BSC area was viewed from nadir by a Spectral Revolution, Inc SR1901 UV-VIS-NIR spectrometer with an 8° FOV, and the container was illuminated with two Tungsten Halogen lights placed about 30° off nadir and 180° apart (Fig. 1a). The reflectance of BSC particles was estimated by comparing the spectrometer measurements of a diffuse-white reflectance standard (an Avian Technologies Fluorilon-99W™) placed in the same location as the BSC container. Such measured reflectance is considered as the hemisphere reflectance with no

units. Five BSC samples and one BSC-free water sample were measured repeatedly to obtain the average reflectance. Although the measurement spectral range was from <350 nm to >1800 nm, data for 400 – 900 nm are presented in Fig. 1b because these are most relevant to the satellite sensors used in this study (see below).

As with any other laboratory tank experiments, although the influence of the container bottom on the measured reflectance can be reduced as with the above settings, some residual influence is inevitable. However, because spectral discrimination requires only the spectral shape rather than reflectance magnitude, the potential residual errors due to the bottom influence should have negligible effects in this work, as shown in the spectral similarity analysis below.

2.3. Field experiment

On 17 December 2019, a small boat was used to search for BSC slicks in the south arm of the GSL. Slicks of various size and density were found at approximately 40.78°N 112.24°W. Digital photos were collected from representative sites (Fig. 2a). Surface reflectance spectra (dimensionless) for each site were measured using the same SR1901 spectrometer as in the laboratory experiment. The measurement followed the standard NASA Ocean Optics protocols for above-water reflectance measurements (Mueller et al., 2003). Specifically, the fiber optic probe was pointed to the target (BSC-free water, BSC slicks, or mixed BSC-water slicks) from a boat operator at 30° nadir with a relative azimuth of ~135° to the sun, and radiance was measured 3 times with 5 spectra collected each time to calculate the average. Similarly, the same probe was pointed to a diffuse-white reflectance standard (an Avian Technologies Fluorilon-99W™) to measure radiance from the standard. Knowing the spectral reflectance of the standard (provided by the manufacture and cross-verified with other reflectance standards in the lab), a ratio between the two measurements, after accounting for the known reflectance of the standard, provided the surface hemisphere reflectance of the target (dimensionless).

2.4. Satellite data

Satellite data from the Visible Infrared Imaging Radiometer Suite (VIIRS)/SNPP, Medium Resolution Imaging Spectrometer (MERIS), and Sentinel-3 Ocean and Land Colour Instrument

were used in this study. VIIRS Red-Green-Blue (RGB) and False-Red-Green-Blue (FRGB) images were produced by NOAA, and inspected through the NOAA OCView online tool (<https://www.star.nesdis.noaa.gov/socd/mecb/color/ocview/ocview.html>; Mikelsons and Wang, 2018; Qi et al., 2020) to determine cloud-free days and to visualize possible BSC slicks. For time series analysis, MERIS (2002 – 2012) and OLCI (2016 – present) data were used because they have more spectral bands (15 for MERIS and 21 for OLCI) than other multi-band sensors and because all bands have the same 300-m nominal resolution. MERIS and OLCI Level-1 data were downloaded from the NASA Goddard Space Flight Center (<https://oceancolor.gsfc.nasa.gov/>), and processed using the software SeaDAS (version 7.5) to obtain Rayleigh corrected reflectance (R_{rc} , dimensionless) for each image pixel. For both MERIS and OLCI, RGB, FRGB, and Normalized Difference Vegetation Index (NDVI) images were generated from R_{rc} using different band combinations. Of these, RGB images were generated using the 665-nm (R), 560-nm (G), and 443-nm (B) bands, while FRGB images were generated using the 665-nm (R), 754-nm (G), and 443-nm (B) bands. The use of the 754-nm band as the green channel was to examine the enhanced NIR reflectance due to floating matters. NDVI was calculated as (Rousel et al., 1973):

$$NDVI = (R_{rc,NIR} - R_{rc,Red}) / (R_{rc,NIR} + R_{rc,Red}). \quad (1)$$

Here, Red and NIR refer to the 665-nm and 754-nm bands, respectively.

2.5. Environmental data

BSC harvest data were obtained from the UDWR (<https://wildlife.utah.gov/>). These data represent total raw biomass harvested by commercial companies, which includes cysts, empty shells, brine shrimp, algae, and other materials.

Salinity data for the south arm were obtained from the Utah Division of Water Quality (https://udwq.shinyapps.io/GSL_data_explorer/). Wind speed, wind direction, and air temperature collected from a station of the Hill Air Force Base (station ID: KHIF; Lat: 41.11, Lon: -111.96) were downloaded from MesoWest (<https://mesowest.utah.edu/>).

2.6. Spectral similarity

Differentiation of certain floating materials (in this case, BSC surface slicks) from other image features in satellite imagery is based on the spectral shape rather than magnitude. This is because in medium-resolution (e.g., 300 m) images such floating materials often occupy a variable small portion of a pixel (Fig. 2a), leading to large variations in the reflectance magnitude in the red and NIR wavelengths (Fig. 2b). The spectral shape, on the other hand, is relatively stable after using a subtraction technique (Fig. 2d).

Here, a numerical measure of the spectral shape similarity is defined through a spectral angle mapper (SAM) index, following Kruse et al. (1993). SAM is the angle between two spectral vectors:

$$\text{SAM (degrees)} = \cos^{-1}[(\sum x_i y_i) / (\sqrt{\sum x_i^2} \sqrt{\sum y_i^2})], \quad (2)$$

where x and y represent two spectra vectors and the summation is for i (band number) from 1 to N . SAM=0° means identical spectral shapes (i.e., two parallel spectra in log space), while SAM=90° means completely different spectral shapes (i.e., two perpendicular spectra).

SAM has been used to differentiate different floating materials (Garaba and Dierssen, 2018; Hu, 2021). In this study, SAM was used to compare the BSC spectral shapes measured from the laboratory experiments, field experiments, and satellite data.

2.7. Segmentation of BSC slicks using a deep learning model

Several confounding factors can make segmentation of BSC slicks in satellite imagery difficult, including thick aerosols, thin clouds, cloud-edge straylight (i.e., 2-3 water pixels adjacent to clouds are “contaminated” by the nearby bright clouds), cloud shadows, sun glint, and other non-BSC surface features (e.g., foam, floating algae). Therefore, effective segmentation of BSC slicks will need to rely on not only spatial context but also spectral contrasts. After several attempts of using popular indexes (e.g., NDVI, floating algae index (FAI, Hu, 2009)), supervised classification, and machine learning such as neural networks, a deep learning (DL) model was deemed most effective. This is because the BSC slicks not only show spectral shapes different from other features but also appear as elongated features in MERIS and OLCI images. The ResUNet DL framework was originally proposed by Xiao et al. (2018) for segmentation of

medical images, but was adapted here for feature extraction from remote sensing images due to its ability to capture spatial context. To help understand the data processing and image segmentation steps, Fig. 3 presents a flow chart, where each step is described below.

2.7.1. Step 1: input and output of the DL model

A set of 82 satellite images, including 25 MERIS and 57 OLCI images, collected from different years and different seasons, were used to train the DL model (Fig. 3). The pixels from the input images were first classified into two groups before being used for model training and evaluation: 1) BSC-containing pixels; 2) others (including pixels of lake water, shallow water, other floating features, clouds, cloud shadows, sun glint, etc.). The classification combined the following steps to delineate BSC-containing pixels:

- 1) Visual inspection of RGB, FRGB, and NDVI images to determine the locations of image slicks;
- 2) For each image slick, spectral shapes of representative pixels were extracted and examined following the approach proposed by Qi et al. (2020). If the spectral shapes showed characteristic of BSC (see Sections 3.1 & 3.2 below), then the slick was designated as a BSC slick;
- 3) For each BSC slick, a rough boundary was manually drawn, within which a gradient method was used to delineate the slick objectively. This step was repeated for all BSC slicks identified in an image.

From all 25 MERIS and 57 OLCI images, a total of 249,866 pixels were determined to be BSC-containing pixels (class 1), with the remaining (3,309,987) being non-BSC pixels (class 2).

The information for both class 1 and class 2 pixels used as the input of the DL model includes normalized R_{rc} and normalized NDVI:

$$nR_{rc} = 255 \times (\log(R_{rc}) - \log(R_{rc \min})) / (\log(R_{rc \max}) - \log(R_{rc \min})) \quad (3)$$

Here, $R_{rc \min}$ and $R_{rc \max}$ are 0.0075 and 0.5, respectively, for R_{rc} data of all 8 bands at 442, 510, 560, 620, 665, 709, 754, and 865-nm. Likewise, NDVI was normalized as:

$$nNDVI = 255 \times (NDVI * 0.5 + 0.5) \quad (4)$$

The purposed of normalizing both R_{rc} and NDVI was to convert floating point values (0.0 – 1.0) to byte values (0 – 255) to improve model performance. Likewise, although $nNDVI$ can be derived from R_{rc} , the use of $nNDVI$ in addition to the normalized R_{rc} as the model input is not redundant but to increase the sensitivity of the model to the red-NIR spectral shape. Similar exercises of using various band combinations in addition to spectral reflectance have been used in other machine learning approaches to estimate global ocean bio-optical parameters (e.g., Hu et al., 2021).

2.7.2. Step 2: Model development and performance evaluation

In summary, the input of the DL model includes the normalized R_{rc} and $nNDVI$ from both BSC-containing pixels and non-BSC pixels, and the DL model training is to obtain the best match between output (which also includes two classes: BSC-containing pixels and non-BSC pixels) and input. This is illustrated in Step 2 of Fig. 3.

After model training, the performance of the model was evaluated by comparing the output (2 classes) and the input (2 classes) using a subset of the images that were not used in model training (Fig. 3, Step 2: model validation). Independent from the 82 model training images, 14 MERIS and 19 OLCI pre-delineated images were used to evaluate the DL model extracted results. The precision, recall, and accuracy were used to measure the model performance:

$$Precision = \frac{TP}{TP+FP} \times 100\% \quad (5)$$

$$Recall = \frac{TP}{TP+FN} \times 100\% \quad (6)$$

$$Accuracy = \frac{TP+TN}{TP+TN+FP+FN} \times 100\% \quad (7)$$

where TP is true positives, TN is true negatives, FP is false positives, and FN is false negatives.

2.8. Quantifying BSC abundance and distribution

After the model training and evaluation, the DL model was applied to a total of 1268 MERIS images and 1049 OLCI images (Step 3 of Fig. 3). In each image, a pixel is classified to be either BSC-containing pixel, non-BSC pixel, or non-observable pixel. Here, the first two classes belong

to the class of “observable”, meaning that the quality of the pixel allows for the determination of whether it contains BSC or not. The “non-observable” pixels include clouds and strong sun glint, where a threshold of $R_{rc}(443) > 0.07$ was used to discard those pixels. The use of a blue band (443 nm) instead of a NIR band or the default “bright pixel” flag of the Level-1 data to discard clouds and strong sun glint is to avoid discarding BSC-containing pixels as these pixels show elevated NIR reflectance, and the threshold of 0.07 was determined from trial and error.

Not every BSC-containing pixel is the same. This is because every BSC-containing pixel is only partially covered by BSC, with the partial coverage (or relative areal density) being expressed as χ (0% - 100%) (Qi and Hu, 2021). To quantify BSC in each image, χ for each BSC-containing pixel needs to be determined using a linear unmixing model (Step 3 in Fig. 3). Specifically, for each BSC-containing pixel, its reflectance, R , can be expressed as:

$$R = \chi R_{BSC} + (1-\chi) R_w \quad (8)$$

R_{BSC} and R_w are the reflectance for “pure” BSC pixel (i.e., $\chi = 100\%$) and BSC-free water pixel, respectively. Then, the difference between R and R_w is

$$\Delta R = R - R_w = \chi(R_{BSC} - R_w) \quad (9)$$

χ can then be derived as

$$\chi = \Delta R / (R_{BSC} - R_w) \quad (10)$$

Here, R can be either surface reflectance, top-of-atmosphere reflectance, or R_{rc} (this work). The subtraction in $\Delta R_{rc} = (R_{rc} - R_{rc,w})$ of Eq. 9 effectively removes aerosol reflectance along with other perturbations (sun glint, thin clouds) because these perturbations are assumed to be the same over BSC-containing pixels and nearby BSC-free pixels. For the same reason, the denominator in Eq. (10), $(R_{rc,BSC} - R_{rc,w})$ is equal to $(R_{BSC} - R_w)$ for surface reflectance. In practice, because the highest contrast between BSC-containing pixels and background water pixels occurs in the NIR wavelengths, the 754-nm MERIS or OCLI band was used to perform the unmixing using Eqs. (8) – (10). In the unmixing, based on the field experiments (Fig. 2b), $R_{BSC}(754) - R_w(754)$ was estimated to be 0.2 (a constant for all images), and χ is scaled linearly between 0% for $\Delta R_{rc}(754)=0.0$ and 100% for $\Delta R_{rc}(754)=0.2$, with $\Delta R_{rc}(754)$ derived from the BSC-containing pixel and nearby water pixels. Here, the assumption is that $R_w(754)$ is $\ll R_{BSC}(754)$ for surface reflectance, which is true unless the water is extremely turbid. Note that

R_w in the above equations is *not* a constant but is from the BSC-free water pixels near the BSC slick, therefore accounting for changes in water quality both spatially and temporally.

After pixel unmixing, BSC abundance and distribution for a given period were determined following the same approach outlined in Qi et al. (2016) for *Ulva* macroalgae. Briefly, the study region was divided into grids of equal size of 4 x 4 pixels (about 1.2 km grid size). For each grid, the mean BSC density (in %) during a given period (e.g., month) was calculated as:

$$f = \frac{1}{N_t} \sum_{i=0}^{N_t} \chi_i \quad (11)$$

where N_t is the number of observable pixels. This is the last step in the flowchart of Fig. 3.

3. Results

3.1. BSC reflectance from laboratory and field experiments

Fig. 1b shows the typical spectral reflectance of the BSC samples corresponding to Fig. 1a. For comparison, overlaid are sample difference spectra extracted from 3 × 3 OLCI pixels (Fig. 11c of Qi et al., 2020). The spectral shapes show several characteristics which, when used altogether, can differentiate BSC slicks from other floating matters. These include

- 1) A sharp increase after 650 nm and elevated reflectance in the NIR
- 2) A monotonic increase after ~550 nm (*in situ* data) or 560 nm (satellite data)
- 3) Two inflection positions around ~550 and ~650 nm (black arrows in Fig. 1b).

These characteristics are apparent in all laboratory-measured spectra. They can also be seen from some of the field-measured spectra when BSC areal density (χ , equivalent to % cover within an image pixel) is high (Fig. 2b). More importantly, the OLCI-derived spectra also show similar characteristics of Fig. 1b, which form the basis for image segmentation using the DL model. Interestingly, these spectral shapes resemble those reported from coral spawn eggs (Yamano et al., 2020), except that the coral spawn eggs (either live or dead) have their first inflection position around 580-590 nm.

Assuming the maximum reflectance spectrum from the laboratory measurements (Fig. 1b, 749 mg) can represent “pure BSC” endmember spectrum and therefore can be used as a reference, SAM between other BSC spectra (Fig. 1b, 340 – 639 mg) and the reference spectrum is $3.3 \pm 2.7^\circ$

(range: $0.1 - 6.6^\circ$), suggesting high similarity (Table 1). Similarly, SAM between the reference and field-measured BSC spectra (after subtraction of water, Figs. 2c & 2d dashed curves) is also very small ($5.1 \pm 0.6^\circ$). Even for the OLCI-derived spectra from the BSC-containing pixels (Fig. 2d solid lines), SAM is still small (6.6° to 10.3°). In contrast, SAM between the BSC reference spectrum and other floating materials, which may or may not be found in typical lake environments, is much higher (Table 1), suggesting relatively unique spectral shapes of BSC slicks as summarized above. Such spectral characteristics can be used to differentiate BSC slicks from other image features.

In addition to the unique shapes, the laboratory experiments suggest that χ appears to increase monotonically with the NIR reflectance, for example at 754 nm (Fig. 1c, where χ is equivalent to biomass density). This is similar to the functionality for *Ulva* (Hu L. et al., 2017), and such a functionality forms the basis for linear unmixing when an image pixel is covered partially by BSC. Indeed, for 300-m resolution pixels, nearly all BSC-containing pixels are covered only partially by BSC, with χ often $< 10\%$.

The spectral shapes from the field experiment in the south arm of the GSL on 17 December 2019 show similar characteristics as those from the laboratory experiment, especially when BSC density is high (Fig. 2b). At lower density, unlike the laboratory-measured spectra, reflectance no longer increases monotonically after ~ 550 nm. This is primarily due to the fact that the lake water is greenish (Fig. 2a) with an apparent reflectance peak around 565 nm (green curve in Fig. 2b), and spectral mixing leads to spectral characteristics of both BSC and lake water. This effect is shown in the “Thin” and “Sparse” spectra of Fig. 2b, corresponding to the digital photos shown in Fig. 2a. The SAM values of these field-measured spectra of mixed BSC and water (i.e., all “Thick”, “Thin”, “Sparse” spectra in Fig. 2a), when the lab-measured BSC reflectance endmember (the “0.75 g” spectrum in Fig. 1b) is used as a reference, are rather large ($20.4 \pm 8.5^\circ$) because of the mixing effect. In contrast, the difference spectra (ΔR) derived from Eq. 9 removes most of the mixing effect and still show monotonic increase after ~ 565 nm (Fig. 2c). Furthermore, when plotted in log scale (Fig. 2d), these spectra are nearly parallel to each other, indicating near-identical spectral shapes regardless of their variable magnitudes due to mixing. Indeed, the SAM values of these spectra, after subtracting the water reference (i.e., ΔR , Fig. 2c

& 2d dashed lines), are much lower ($5.1 \pm 0.6^\circ$, Table 1) than the SAM value of the original spectra (R), suggesting that the BSC spectral shapes are retained in ΔR as opposed to R . From Eq. 9, this effect is easy to understand, as the spectral shape in ΔR is determined equally by R_{BSC} and R_{W} . When they are both stable, the spectral shape is also stable, but the magnitude in ΔR is modulated by χ . Furthermore, when R_{W} is $\ll R_{\text{BSC}}$ in certain wavelengths (e.g., red – NIR), the spectral shape is dominated by R_{BSC} regardless of χ .

3.2. BSC reflectance from MERIS and OLCI images

Fig. 4a shows an OLCI FRGB image collected on 17 December 2019, where surface slicks in both the north arm and the south arm can be visually identified. The north arm has a salinity of ~ 300 g/L (compare: salinity of most seawater is ~ 35 - 36 g/L), making it a suitable environment for halobacteria, which tend to produce white foam on the water surface (Baxter 2018). Indeed, OLCI spectra extracted from several slick pixels show relatively flat reflectance shape (Figs. 4b & 4c), suggesting possible white foam. In contrast, reflectance spectra extracted from slick pixels in the south arm (salinity ~ 140 g/L) have different shapes than from the north arm (Figs. 4d & 4e), where a sharp increase is found at wavelengths $> \sim 560$ nm. Indeed, when overlaid on the spectra collected from the *in situ* experiment (Fig. 2d), these spectra show high similarity, suggesting that the image slicks in the south arm are from BSC aggregations. Spectral similarity test using the SAM also suggests the same, as SAM values for these OLCI spectra are $8.4 \pm 1.9^\circ$, as compared with the non-BSC SAM values of $23.4 \pm 2.8^\circ$ (Table 1). Different reflectance magnitudes indicate different BSC-water mixing ratios (χ). Assuming that $\Delta R_{\text{rc}}(754) = 0.2$ corresponds to 100% BSC coverage (i.e., $\chi = 100\%$) (Eq. 10), the three spectra suggest 5%, 10% and 25% of partial BSC coverage within the 300-m OLCI pixel, respectively.

Similar spectral shapes were also obtained from MERIS images for the south arm. Therefore, the unique shapes were used to identify BSC-containing pixels and non-BSC pixels, whose ΔR_{rc} and NDVI data were used to train the DL model to delineate BSC slicks (Section 2.7), with results presented below.

3.3. Extraction of BSC slicks through the DL model

Fig. 5 shows two examples from MERIS and OLCI, respectively, on how the DL model extracted the BSC slicks in the south arm of the GSL. The FRGB images in Figs. 5a & 5b show image slicks, and their representative spectra in Figs. 5g & 5h show typical BSC reflectance spectral shapes, as compared with those in Fig. 4 and from the laboratory and field experiments (Figs. 1 & 2). After proper training, the DL model identified nearly all image slicks as BSC slicks (Figs. 5c & 5d). In contrast, the use of the NDVI images alone (Figs. 5e & 5f) cannot distinguish BSC slicks from thin clouds (outlined in red circles), not to mention the difficulty in selecting a universal threshold to delineate BSC slicks from multiple images. Due to the space limit, the images are shown here for illustration purpose only, while the full-size images corresponding to Figs. 5a – 5d can be found in supplemental Figs. S1a – S1d, respectively.

After BSC slick delineation, BSC areal density (χ) in each BSC-containing pixel was determined using Eq. 10. In the two examples of Figs. 5c & 5d, χ is color coded between 0% and 5%.

The performance of the DL model was evaluated using 33 randomly selected (14 MERIS and 19 OLCI), pre-delineated images which were not included in the model training. In this study, the precision, recall, and accuracy of the model are 95.7%, 91.0%, and 88.0%, respectively. Such a performance was considered to be acceptable for BSC slick detection and long-term time series analysis.

3.4. BSC abundance and distributions

A total of 1268 of MERIS and 1049 of OLCI images covering the GSL were used to determine BSC abundance and spatial/temporal distributions between 2002 and the present. The DL model was applied to each image to delineate the BSC slicks, and each BSC-containing pixel was unmixed using Eq. (10), and then aggregated to the predefined grids to estimate mean monthly density (%) in each grid using Eq. (11). Because each grid has a finite size (about $1.2 \times 1.2 \text{ km}^2$), the density can be easily converted to BSC abundance (km^2) in each grid. An integration of all grids results in the total BSC abundance (km^2) for the south arm of GSL.

The temporal changes of BSC abundance in the south arm of the GSL, at monthly, climatological monthly, and annual scales, is shown in Figs. 6a, 6b, and 6c, respectively. Despite the 4-year gap (May 2012 – April 2016), the combined use of MERIS and OLCI yielded a 15-year record of BSC

abundance between 2002 and 2020, which showed clear seasonality and inter-annual changes. The seasonality pattern in Fig. 6b shows a primary peak in spring (April – May) and a secondary peak in fall (October – November), with minimal abundance in July – August. On annual scale, although there is substantial inter-annual variability, there appears an increasing trend in recent years (Fig. 6c).

The BSC abundance is not equally distributed in the south arm of the lake, but with more BSC in the south and west, especially during the peak months of April – May and October – November (Fig. 7a). In contrast, the northeast of the south arm shows little or no BSC. For the entire month of July and August, there are very few BSC slicks found from the MERIS or OLCI images.

One may question whether these observations are statistically meaningful. Fig. 7b shows the number of valid observations (i.e., valid image pixels) in each 1.2-km grid in each climatology month. There is a clear seasonality, with maximal observations during summer (June – August) and minimal observations during winter (December – February). Even during the winter months, the number of valid observations is still > 500 for most grids, thus the results for climatological months appear to be statistically robust. For each calendar month, during the winter months the number of valid observations in each grid may be reduced to $500/15 \approx 33$, suggesting that although the statistics is less robust than for the corresponding climatological months, it is still meaningful.

4. Discussion

4.1. Spectral shapes of BSC

From both laboratory and field measurements, BSC particles show unique spectral shapes, including a sharp increase after ~ 650 nm, a monotonic increase after ~ 550 nm, and two inflection positions (~ 550 and ~ 650 nm). These spectral characteristics are different from all other reported floating matters in either lakes or oceans (Qi et al., 2020). One exception is perhaps the case for coral spawn eggs (Yamano et al., 2020). However, the first inflection position in reflectance of coral eggs (either live or dead) is around 589-590 nm, and corals do not live in the GSL or other salt lakes, therefore can be ruled out as possible sources of the image slicks. The similarity test between BSC and other possible floating materials in lakes indeed suggests that BSC spectral shapes are different from all other floating materials (Table 1).

Therefore, future efforts in searching for BSC slicks in other salt lakes may use such spectral characteristics as the BSC signatures.

In the above observations, the BSC spectral shapes are only retained in the difference spectra (ΔR) rather than in R from either field measurements or satellite images. This is because of the small size (relative to either the field-of-view of the field instruments or image pixel size) of BSC patches, leading to χ often being $< 5\%$ (Figs. 5c & 5d). In such cases, the spectral shape in R is dominated by water rather than by BSC ($1-\chi \gg \chi$, see Eq. 8), but the spectral shape of ΔR is determined equally by water and BSC (χ for both, see Eq. 9). In the red and NIR wavelengths where R_w is $\ll R_{BSC}$, the spectral shape of ΔR is dominated by BSC. The concept of spectral difference has actually been introduced by Gower et al. (2006) when discriminating floating *Sargassum* against other image features, and has been elaborated in Qi and Hu (2021) when differentiating different types of floating vegetation and in Hu (2021) when differentiating floating vegetation from non-vegetation. Without the use of ΔR , BSC reflectance shape measured in the field (Fig. 2b) can be very different from those determined in the laboratory (Fig. 1b), with SAM values being $20.4 \pm 8.5^\circ$. In contrast, SAM values of the corresponding ΔR from the same BSC measurements are much lower ($5.1 \pm 0.6^\circ$, Table 1), suggesting the effectiveness ΔR in retaining the BSC spectral shapes regardless of the magnitude of χ . This is why BSC spectral shapes in this study are examined through ΔR . The same argument also applies to all other floating matters, especially when their sub-pixel coverage (χ) is very small (Hu, 2021).

4.2. Algorithm design

Because χ is often much smaller than 100% and only ΔR can retain the spectral shape of floating matters, detecting and quantifying floating materials are different from estimating water-column properties such chlorophyll-a concentrations or turbidity. In this work, we followed previous works to quantify floating algae (Gower et al., 2006; Hu, 2009; Qi et al., 2016; Hu L. et al., 2017 & 2019) or materials using red-edge based indexes such as MCI (Maximum Chlorophyll Index, Jim Gower and co-workers), FAI (Floating Algae Index, Hu and coworkers), or MPH (Maximum Peak Height, Matthew et al., 2012), while the detection of BSC

presence/absence is based on a deep learning model and lab/field measured BSC spectral shapes. Although detecting a spatial anomaly can utilize an index such as NDVI or a green/red band ratio (e.g., Yamano et al., 2020), spectral discrimination of the detected spatial anomalies is not trivial because the spectral shape is dominated by water (often > 95% of a pixel, Figs. 5c & 5d). This is why a DL model was used to account for both spectral shapes and spatial context of the slicks, as similar models have been used successfully in remote sensing applications such as road extraction and land use (Zhang et al., 2018; Shamsolmoali et al., 2019). If a non-BSC feature is falsely recognized by the DL model as a BSC feature, the DL model can be retrained by including the non-BSC feature as the additional input, thus avoiding similar false-positive detection. For this reason, the DL model requires extensive training for the specific sensor and study region, which is labor intensive. When transferred to other regions, the model also requires retraining to account for the different water and atmospheric environments. On the other hand, changes in chlorophyll-a or turbidity do not significantly alter the spectral contrast between BSC-containing pixels and BSC-free pixels, as most of the contrast comes from the red-NIR wavelengths even for turbid waters (see Fig. 2b). Therefore, although the background water spectra may change over time because of different chlorophyll-a and turbidity, as long as the training images encompass these different scenarios, they will not affect the DL model performance because the training can take care of the potential impact of such changes on the spectral contrast. An example is shown in the supplemental Fig. S2 to demonstrate why this is the case. In the same FRGB image of Fig. S2a, both BSC slicks and non-BSC features are identified. Due to their different spectral shapes (Fig. S2b), the DL model correctly identified the BSC slicks (color coded in Fig. S2a) without false positive detection of the non-BSC features.

Once BSC slicks are detected by the DL model, quantifying BSC % cover (or biomass density) is straightforward using Eqs. (10) and (11). This is similar to quantifying macroalgae % cover (Qi et al., 2016 & 2017). Therefore, although the DL model can only classify the presence/absence of BSC in individual pixels, the unmixing equations can quantify the BSC amount, thus leading to quantitative detection.

For the same reasons supporting the accurate spectral discrimination and spectral unmixing, one major drawback of the approach (including the DL model) is its complexity that makes it

difficult to transfer to other lakes, especially for managers and other non-specialists. Such a difficulty may be circumvented by using some simple indexes such as MPH (Matthew et al., 2012) or alternative FAI (AFAI, Qi et al., 2018) for lakes with mono-species of algae (e.g., cyanobacteria) forming surface scums. Some of these simple indexes such as NDVI or FRGB are available through the Sentinel Hub EO Browser and NOAA OCView online tools, which may provide a fast, qualitative presence/absence detection. However, when more than one type of floating algae or floating matters coexist in a lake, more sophisticated algorithms such as the DL model are required to improve detection.

4.3. Product uncertainties

Direct field validation of detection (presence/absence) and quantification (% cover or χ) of any small features (relative to image pixel size) is always difficult. These features can include oil slicks, floating vegetation, marine debris, and other materials. Therefore, very few, if any, papers have used direct field validations, especially for the quantification, as it is nearly impossible to relate a large pixel to much smaller, patchy features except for the presence/absence validation. However, there are two ways of indirect (i.e., non-field based) validation. One is through inspection of the spectral shapes of the classified pixels, leading to several statistical measures (Eqs. 5-7) of the presence/absence classification results. The quantification is based on physical principles (surface light from different parts of a pixel is additive), therefore should be accurate with quantifiable uncertainties. Two, higher-resolution data can be used as a surrogate of ground truth to evaluate results from 300-m resolution data. These considerations have been discussed in other studies when using medium-resolution data to estimate χ of surface features. For example, using 2-m resolution of WFV/GF-1 data, floating algae coverage derived from 250-m resolution MODIS/Terra and MODIS/Aqua images have been evaluated (Hu L et al., 2019). From 17 concurrent and co-located image pairs, Root-Mean-Square differences between MODIS and GF-1 data were found to be 11%, with a mean bias of 5% (Table 3 of Hu L et al., 2019). Because the physical principles of linear unmixing is the same for BSC slicks, it is believed that the derived BSC % cover contains similar uncertainties, which are relatively small as compared with either BSC seasonality or inter-annual changes (Fig. 6).

Because two sensors were used in forming the time series, could some of the changing patterns be due to inconsistency between MERIS and OLCI in either radiometric calibration or atmospheric correction? Such a possibility should actually be very small for several reasons: 1) OLCI is a follow-on sensor of MERIS with very similar band settings; 2) the BSC discrimination (i.e., presence/absence detection) depends only on the spectral shape of $\Delta R_{rc}(\lambda)$ as opposed to the magnitude of either $R_{rc}(\lambda)$ or $\Delta R_{rc}(\lambda)$; 3) the BSC quantification (χ) only depends on $\Delta R_{rc}(754)$. These latter two steps essentially minimize the impact of any potential cross-sensor inconsistency in either radiometric calibration or atmospheric correction. For example, because the atmosphere and viewing geometry over both BSC slicks and adjacent water pixels are the same, effects of aerosols, sun glint, and thin clouds are effectively removed in the difference spectra (i.e., $\Delta R_{rc}(\lambda)$). For this reason (i.e., reflectance difference rather than reflectance is used), a 3% error in the top-of-atmosphere (TOA) radiance will lead to ~3% error in ΔR_{rc} . This contrasts with the traditional pixel-wise atmospheric correction approaches, where a 3% TOA error can lead to 30% surface reflectance error because most of the TOA signal comes from the atmosphere. In reality, the absolute uncertainty of TOA radiometric calibration is believed to be < 3% (after vicarious calibration, the relative uncertainty is < 1%) (Barnes et al., 2020). Therefore, such possible cross-sensor inconsistency in either TOA calibration or atmospheric correction will unlikely impact the long-term BSC patterns derived from the two sensors. Indeed, the inter-annual changes from one sensor (OLCI) appears to be higher than the cross-sensor changes, also supporting the above argument.

Finally, the estimate of χ depends directly on the assumption that $R_{BSC}(754) = 0.2$ for $\chi = 100\%$. This assumption is based on both the laboratory experiment (Fig. 1b) and field measurement (Fig. 2b). In reality, $R_{BSC}(754)$ for $\chi = 100\%$ could be higher than 0.2, leading to uncertainties in both the estimated χ at pixel level and the estimate BSC coverage (km^2) for the study region. However, this possibility will change χ equally for all pixels, and will similarly change the mean monthly or annual BSC coverage equally in all months and years. Therefore, such a possibility will only result in a systematic small bias rather than random, time-dependent errors, thus will not change either the seasonality pattern (Fig. 6b) or long-term pattern (Fig. 6c) in the estimated BSC coverage. Overall, after considering all possible factors above, we believe that all

these possible uncertainties would not alter either the seasonality pattern or the long-term pattern.

4.4. Impacts of environmental factors and human activities on BSC spatial distribution patterns and temporal changes

Despite the importance of BSC to the GSL's ecology and local industry, to date, satellite remote sensing has only been used to study the lake's water environment (e.g., temperature) (Crosman & Horel, 2009; Hall et al., 2021; Hansen et al., 2017; Hung & Wu, 2005). The results presented above therefore represent the first of its kind to directly estimate surface BSC abundance and their spatial/temporal distribution patterns. While understanding these patterns requires an integrated study involving field measurements and numerical models, we attempt to explain such patterns using readily available environmental data.

4.4.1. Spatial distribution patterns

Fig. 8a shows that wind is mostly from the north and northwest for every season between 2002 - 2020. This is especially true for high winds (>4 m/s). The dominant wind direction explains why most BSC slicks were found in the south and west of the south arm (Fig. 7a), as the wind forcing, after considering the Coriolis effect, would transport the surface BSC particles toward south and southwest.

4.4.2. Seasonality

Two peaks are found in the BSC seasonal cycles, in April – May and October – November, respectively. Although the peaks also occur in other months when monthly data in individual years are examined, when all years are combined, the climatology monthly data show two distinctive peaks only. Such a seasonality is consistent with those obtained from limited field observations that spanned 1-2 years (Stephens & Gillespie, 1976; Wurtsbaugh and Maciej Gliwicz, 2001). While spawning of brine shrimp is continuous, the amount of brine shrimp may be influenced by salinity, temperature, food sources, and predation (Van Stappen 1996). Both wind and salinity are relatively stable in different months (Fig. 8b), thus may be ruled out as

possible causes of the BSC seasonality. While temperature shows a strong seasonality with winter lows and summer highs, it is unclear whether/how temperature has a direct impact on shrimp ecology and therefore BSC abundance. Of all these environmental factors, food availability and brine shrimp reproduction are perhaps the most plausible reasons behind the two observed seasonal peaks. *Dunaliella* serves as the main food source for brine shrimp in the GSL. Field measurements showed that the peak growth of *Dunaliella* is in March and April, thus providing sufficient food for brine shrimp (Stephens & Gillespie, 1976; Wurtsbaugh & Maciej, 2001) after the initial hatching before spring, leading to high BSC abundance in April - May. As the amount of brine shrimp increases toward the summer, food (i.e., *Dunaliella*) may be gradually depleted (Stephens & Gillespie, 1976; Wurtsbaugh & Maciej, 2001), resulting in a decrease of brine shrimp populations during one or more reproductions and therefore reduced BSC abundance during summer, after which brine shrimp from a new generation gradually recovered to lead to a secondary BSC peak in fall. Such bottom-up effect for the primary peak and top-down effect for the secondary peak resemble the mechanisms behind the primary phytoplankton peak and secondary phytoplankton peak in the North Atlantic. Ideally, an accurate long-term data record of *Dunaliella* abundance may be used to test the bottom-up hypothesis. However, such data is currently not available from either field measurements or satellite remote sensing, and developing *Dunaliella*-specific remote sensing algorithms is technically challenging due to lack of field data. Likewise, remote sensing of chlorophyll-a concentrations in the GSL has also been limited, making it difficult to assess long-term changes of phytoplankton. To date, the only remote sensing attempt was made by Bradt (2012), where hyperspectral reflectance and chlorophyll-a data were used to formulate empirical band-ratio chlorophyll-a algorithms. Given the unknown bio-optical properties of other optically active constituents (e.g., colored dissolved organic matter, suspended solids, shallow bottom), band-ratio algorithms perhaps contain large uncertainties when time-series of chlorophyll maps are to be derived. Compared to many other lakes, the GSL has been understudied in terms of remote sensing. In the future, more effort is required to address the technical challenges in algorithm development and product validation through targeted and coordinated field

measurements, especially on chlorophyll-a and *Dunaliella*, from which the water environment can be better understood in order to test the above hypothesis.

4.4.3. Inter-annual changes

There are two apparent patterns in the 2002 – 2020 BSC time-series data in Fig. 6c: significant inter-annual variability, and an increasing trend in recent years. The trend was calculated using the modified Mann Kendall test (Hussain and Mahmud, 2019), which was originally proposed by Mann (1945). According to the test, for the combined MERIS and OLCI (2002 – 2020), the increasing trend is not statistically significant but still apparent ($p = 0.096$). For the OLCI data alone (2016 – 2020), the increasing trend is statistically significant ($p = 0.028$). Are any of these patterns a result of environmental changes due to climate variability, or human activities such as BSC harvesting?

Indeed, the GSL has undergone dramatic changes over the past decades, for example its area has shrunk, and its salinity has increased (Wurtsbaugh et al., 2017). One may speculate whether changes in salinity may have played a role in explaining the long-term BSC patterns. However, since 2002, the salinity of the south arm has not changed drastically but remained at about 140 g/L, which is the optimum salinity for brine shrimp reproduction (Vanhaecke et al., 1987). Fig. 8c shows that while salinity fluctuated between 120 and 150 g/L since 2010, the fluctuation does not correspond to the inter-annual BSC changes, nor can it explain the recent BSC increasing trend. Likewise, air temperature and winds do not appear to be able to explain the inter-annual BSC changes either. Then, do the BSC patterns mimic BSC harvest in the past two decades?

With the expansion of global aquaculture production, the market demand for BSC is increasing (Baxter & Butler, 2020). Commercial harvest of BSC in the GSL started from the 1950s, and it is now the most important source of BSC supply worldwide. In order to have a sustainable industry while keeping a healthy lake ecosystem, the Utah government has implemented regulations on BSC harvest (Administrative rule R657-52), for example by expending or restricting the BSC harvest season according to field surveys of BSC abundance. Fig. 6c shows that the amount of BSC harvest has been on the rise since 2003, and the current harvest scale is

about 5-8 times higher than in 2003. From the management data maintained by the Great Salt Lake Ecosystem Program at the Utah Division of Wildlife Resources, this appears to be a result of improved harvest technology and improved coordination between industry and management. Other than this, similar to the environmental factors, BSC harvest does not appear to show any pattern corresponding to the annual fluctuations in the satellite-derived BSC amount (Fig. 6c). On the other hand, increased harvest in 2018 – 2019 is accompanied with increased BSC in the following spring of 2019 – 2020, suggesting that the management regulations have been effective to sustain the brine shrimp population to support an increasing BSC harvest industry. In any case, whether or not the increasing trend of BSC, which likely supports sustainable BSC harvest, will continue in the future can be evaluated with the approach outlined here with satellite remote sensing data.

4.5. Global implications

Although the focus of this study is on the GSL, because of the availability of satellite data at the global scale, the study has significant implications to other salt lakes.

It has been shown that lakes with salinity greater than 70 g/L are suitable for the growth and reproduction of brine shrimp (Van Stappen, 1996). There are many salt lakes worldwide with salinities above 70 g/L. Do these lakes also show image slicks that can be spectrally diagnosed to be BSC slicks? An online search using the NOAA OCView tool (Mikelsons and Wang, 2018; Qi et al., 2020) found image slicks in at least three other large salt lakes: the Aral sea, Lake Urmia, and the Dead Sea (Figs. 9a – 9c).

The greenish slicks in the FRGB images of these lakes are clearly visible (Figs. 9a – 9c), especially when viewed in full size in the supplemental materials (Fig. S3). Reflectance spectra of Figs. 9d – 9f from some sample pixels of these slicks in Figs. 9a – 9c show spectral shapes that are similar to those of the BSC slicks found in the GSL, with a sharp increase after 560 nm and enhanced NIR reflectance. SAM values between these spectra and the BSC reference spectrum are all < 13°. Such characteristics strongly suggest that these image slicks are also due to surface aggregations of BSC. Although no remote sensing study of BSC can be found in the literature, the presence of brine shrimp in these three lakes has been studied using field measurements

(Arashkevich et al., 2009; Asem et al., 2012; Haas&Goldschmidt, 1946), indirectly confirming the findings here.

Similar to the GSL, the three lakes have also experienced declining water levels, shrinking lake surface areas, and increased salinities in recent decades (Wurtsbaugh et al., 2017). Currently, salinity is ~100 g/L in the Aral Sea (Aladin et al. 2009), ~250 g/L in the Dead Sea (Mor et al., 2018), and >300 g/L in Lake Urmia (Asem et al., 2012). Studies based on field data showed that brine shrimp can hardly survive in waters with salinity of > 250 g/L (Van Stappen, 1996), yet satellite images over Lake Urmia and the Dead Sea, where salinity is about or greater than 250 g/L, show many BSC slicks. This finding therefore provides new information on the salinity range suitable for brine shrimp, as they can apparently still grow and reproduce under extreme conditions (salinity > 300 g/L). On the other hand, in lakes with low salinities such as Qinghai Lake and the Caspian Sea, satellite images did not reveal any image slicks with spectral characteristics resembling BSC.

Nevertheless, while a systematic evaluation of BSC slicks in all salt lakes around the world can be conducted in the future, the examples above demonstrate the feasibility of the proposed method in finding BSC slicks and quantifying BSC abundance in major salt lakes as long as the lakes are large enough to show up in medium-resolution satellite imagery. Furthermore, how BSC abundance changed in other salt lakes over the past decades under a changing climate and increased human activities deserves more research.

Finally, the study used MERIS and OLCI multi-band satellite sensors to classify and quantify BSC slicks and to quantify BSC abundance. In a practical sense, other multi-band sensors such as Landsat series (30-m resolution) or Sentinel-2 sensors (10 – 20 m resolution) can also be used. Although they have fewer spectral bands, the spectral difference technique (Eq. 9) still enables the BSC spectral characteristics being revealed in the red and NIR Landsat bands, making it possible for both detection and quantification at greater details than provided by MERIS or OLCI. Inspection of Landsat and Sentinel-2 images confirmed such a capacity. One possible drawback is their less frequent coverage than the medium-resolution OLCI sensors, so all these sensors may be combined, as the inclusion of such high-resolution data may detect smaller BSC slicks,

thus reducing uncertainties from the medium-resolution results. We expect to carry out such a sensor-fusion experiment in the near future using sensors of mixed resolutions.

5. Conclusions

In the past, for fisheries studies, satellite remote sensing has been used primarily to assess the aquatic environment. Here, we demonstrate that it is possible to detect aggregations and quantify abundance of brine shrimp cysts (BSC) on the water surface using satellite remote sensing. The use of long-term MERIS and OLCI data also reveals spatial distribution patterns and long-term variations of BSC abundance in surface waters of the Great Salt Lake, where such information is difficult to obtain through limited field surveys. As the GSL is the largest source for commercial BSC products, the findings here may help understand the lake's ecology and help make BSC harvest management decisions. Likewise, the demonstrated feasibility suggests that a systematic evaluation of BSC abundance in major salt lakes worldwide may be carried out using multiple satellite sensors to understand how brine shrimp populations are affected by climate variability and human activities.

Acknowledgements

This work was supported by the National Natural Science Foundation of China (No. 41806208 & No. 42076180 (Qi); No.42071341 & NO.41771366 (Ma)) and the U.S. NOAA (U.S. NOAA, NA15OAR4320064) (Hu). We thank Mr. Alex Manos for collecting reflectance data from the Great Salt Lake. We thank NASA and ESA for providing satellite data, and thank Dr. Mengqiu Wang for her assistance in developing the DL model. Four anonymous reviewers provided comments and suggestions to help improve the presentation of this work, whose effort is appreciated.

Notations

BSC	Brine shrimp (<i>Artemia</i>) cysts
GSL	Great Salt Lake
R	Reflectance (dimensionless)
R_{rc}	Reflectance after Rayleigh Correction (dimensionless)

R_{BSC}	Reflectance of BSC at 100% coverage
R_w	Reflectance of BSC-free water, often derived from pixels near the BSC slicks
ΔR	Difference between BSC-containing and BSC-free water pixels (dimensionless)
χ	Subpixel BSC coverage (%), also called areal density
MERIS	Medium Resolution Imaging Spectrometer (2002 – 2012)
OLCI	Ocean and Land Colour Instrument (2016 – present)
VIIRS	Visible Infrared Imaging Radiometer Suite (2012 – present)
MODIS	Moderate Resolution Imaging Spectroradiometer (2000 – present)
SAM	Spectral Angle Mapper ($0^\circ - 90^\circ$), an index to measure the similarity of spectral shapes between two reflectance vectors. $\text{SAM} = 0^\circ$ indicates identical spectral shapes, while $\text{SAM} = 90^\circ$ indicates completely different spectral shapes
FAI	Floating Algae Index (dimensionless), a measure of the red-edge reflectance of vegetation through the use of band subtraction
AFAI	Alternative FAI, which uses several red and near-infrared bands to measure the red-edge reflectance in the absence of short-wave infrared bands
MPH	Maximum Peak Height, a measure of chlorophyll fluorescence and red-edge reflectance through the use of maximum reflectance from several bands
NDVI	Normalized Difference Vegetation Index (dimensionless), a measure of the red-edge reflectance of vegetation through the use of band ratio.
FRGB	False-color Red-Green-Blue, where an NIR band is used in the green channel.
DL	Deep Learning, one type of artificial intelligence and sub-category of machine learning. DL models use complex, multi-layered neural networks to account for spectral and spatial context of the input data, which require more extensive training and are more computationally intensive than other machine learning techniques.
UNet	A DL technique based on a convolutional neural network, originally developed for segmentation of medical images.
ResUNet	A type of UNet that can take advantage of both the architecture of convolutional neural network and the deep residual learning, also called Deep Residual UNet.

- EO Browser An online image visualization tool developed by the European Space Agency (<https://apps.sentinel-hub.com/eo-browser/>)
- OCView An online image visualization tool developed by the U.S. NOAA (<https://www.star.nesdis.noaa.gov/socd/mecb/color/ocview/ocview.html>)

Reference

- Aladin, N. V., Plotnikov, I. S., Micklin, P., & Ballatore, T. (2009). Aral Sea: Water level, salinity and long-term changes in biological communities of an endangered ecosystem-past, present and future. *Natural Resources and Environmental Issues*, 15(1), 36.
- Arashkevich, E.G., Sapozhnikov, P.V., Soloviov, K.A., Kudyshkin, T.V., & Zavialov, P.O. (2009). Artemia parthenogenetica (Branchiopoda: Anostraca) from the Large Aral Sea: Abundance, distribution, population structure and cyst production. *Journal of Marine Systems*, 76, 359-366.
- Asem, A., Mohebbi, F., & Ahmadi, R. (2012). Drought in Urmia Lake, the largest natural habitat of brine shrimp Artemia. *World aquaculture*, 43, 36-38.
- Barnes, B. B., Hu, C., Bailey, S. W., & Franz, B. A. (2021). Sensitivity of Satellite Ocean Color Data to System Vicarious Calibration of the Long Near Infrared Band. *IEEE Transactions on Geoscience and Remote Sensing*, 59(3), 2562-2578. <https://doi.org/10.1109/TGRS.2020.3000475>
- Baxter, B.K. (2018). Great Salt Lake microbiology: a historical perspective. *International microbiology : the official journal of the Spanish Society for Microbiology*, 21, 79-95.
- Baxter B.K., Butler J.K. (2020) Climate Change and Great Salt Lake. In: Baxter B., Butler J. (eds) Great Salt Lake Biology. Springer, Cham. https://doi.org/10.1007/978-3-030-40352-2_2
- Belovsky, G. E., & Perschon, W. C. (2019). A management case study for a new commercial fishery: brine shrimp harvesting in Great Salt Lake, Utah, USA. *Ecological Applications*, 29(3), e01864. <https://doi.org/https://doi.org/10.1002/eap.1864>
- Bradt, S. R. (2012). Development of bio-optical algorithms to estimate chlorophyll in the Great Salt Lake and New England lakes using in situ hyperspectral measurements. Doctoral Dissertations. 683, <https://scholars.unh.edu/dissertation/683>.
- Belovsky, G. E., Stephens, D., Perschon, C., Birdsey, P., Paul, D., Naftz, D., Baskin, R., Larson, C., Mellison, C., Luft, J., Mosley, R., Mahon, H., Van Leeuwen, J., & Allen, D. V. (2011). The Great Salt Lake Ecosystem (Utah, USA): long term data and a structural equation approach. *Ecosphere*, 2(3), art33. <https://doi.org/https://doi.org/10.1890/ES10-00091.1>
- Crosman, E.T., & Horel, J.D. (2009). MODIS-derived surface temperature of the Great Salt Lake. *Remote Sensing of Environment*, 113, 73-81.
- Dierssen, H. M. (2019). Hyperspectral Measurements, Parameterizations, and Atmospheric Correction of Whitecaps and Foam From Visible to Shortwave Infrared for Ocean Color Remote Sensing [Original Research]. *Frontiers in Earth Science*, 7(14). <https://doi.org/10.3389/feart.2019.00014>
- Garaba, S.P., & Dierssen, H.M. (2018). An airborne remote sensing case study of synthetic hydrocarbon detection using short-wave infrared absorption features identified from marine-harvested macro- and microplastics. *Remote Sens. Environ.* 205, 224–235.
- Gower, J., King, S., Borstad, G., & Brown, L. (2005). Detection of intense plankton blooms using the 709 nm band of the MERIS imaging spectrometer. *International Journal of Remote Sensing*, 26, 2005-2012.
- Gower, J., Hu, C., Borstad, G., & King, S. (2006). Ocean color satellites show extensive lines of floating Sargassum in the Gulf of Mexico. *IEEE Transactions on Geoscience and Remote Sensing*, 44, 3619–3625.

15. Haas, G., & Goldschmidt, E. (1946). A Decaploid Strain of *Artemia Salina*. *Nature*, *158*, 239-239.
16. Hall, D.K., O'Leary, D.S., DiGirolamo, N.E., Miller, W., & Kang, D.H. (2021). The role of declining snow cover in the desiccation of the Great Salt Lake, Utah, using MODIS data. *Remote Sensing of Environment*, *252*, 112106
17. Hammer, U.T. (1978). The saline lakes of Saskatchewan III. Chemical characterization. *Internationale Revue der gesamten Hydrobiologie und Hydrographie*, *63*, 311-335.
18. Hansen, C. H., Burian, S. J., Dennison, P. E., & Williams, G. P. (2017). Spatiotemporal Variability of Lake Water Quality in the Context of Remote Sensing Models. *Remote Sensing*, *9*(5), 409. <https://www.mdpi.com/2072-4292/9/5/409>
19. Hussain, M. M., & Mahmud, I. (2019). pyMannKendall: a python package for non parametric Mann Kendall family of trend tests. *Journal of Open Source Software*, *4*(39), 1556.
20. Hu, C. (2009). A novel ocean color index to detect floating algae in the global oceans. *Remote Sensing of Environment*, *113*, 2118-2129.
21. Hu, L., Hu, C., & Ming-Xia, H. (2017). Remote estimation of biomass of *Ulva prolifera* macroalgae in the Yellow Sea. *Remote Sensing of Environment*, *192*, 217-227.
22. Hu, L., K. Zeng, C. Hu, and M-X. He (2019). On the remote estimation of *Ulva prolifera* areal coverage and biomass. *Remote Sens. Environ.*, *223*:194-207. <https://doi.org/10.1016/j.rse.2019.01.014>.
23. Hu, C. (2021). Remote detection of marine debris using satellite observations in the visible and near infrared spectral range: Challenges and potentials. *Remote Sens. Environ.*, *259*, 112414, <https://doi.org/10.1016/j.rse.2021.112414>
24. Hu, C., Feng, L., & Guan, Q. (2021). A Machine Learning Approach to Estimate Surface Chlorophyll a Concentrations in Global Oceans From Satellite Measurements. *IEEE Transactions on Geoscience and Remote Sensing*, *59*(6), 4590-4607. <https://doi.org/10.1109/TGRS.2020.3016473>
25. Hung, M.C., & Wu, Y.H. (2005). Mapping and visualizing the Great Salt Lake landscape dynamics using multi - temporal satellite images, 1972 – 1996. *International Journal of Remote Sensing*, *26*, 1815-1834
26. Kruse, F, A., A.B. Lefkoff, J.W. Boardman, K.B. Heidebrecht, A.T. Shapiro, P.J. Barloon, A.F.H. Goetz (1993). The spectral image processing system (SIPS)—interactive visualization and analysis of imaging spectrometer data. *Remote Sensing Environ.*, *44*:145-163.
27. Mann, H. B. (1945). Nonparametric tests against trend. *Econometrica: Journal of the econometric society*, *245*-259.
28. Matthews, M. W., S. Bernard, and L. Robertson (2012). An algorithm for detecting trophic status (chlorophyll-a), cyanobacterial-dominance, surface scums and floating vegetation in inland and coastal waters. *Remote Sens. Environ.*, *124*:637-652. doi:10.1016/j.rse.2012.05.032.
29. Mikelsons, M., Wang, M., 2018. Interactive online maps make satellite ocean data accessible. *Eos* *99*. <https://doi.org/10.1029/2018EO096563>.
30. Mor, Z., Assouline, S., Tanny, J., Lensky, I.M., & Lensky, N.G. (2018). Effect of Water Surface Salinity on Evaporation: The Case of a Diluted Buoyant Plume Over the Dead Sea. *Water Resources Research*, *54*, 1460-1475.
31. Mueller JL, Davis C, Arnone R, Frouin R, Carder K, Lee ZP, Steward RG, Hooker S, Mobley CD & McLean S. 2003. Above-water radiance and remote sensing reflectance measurement and analysis protocols, in: *Ocean Optics Protocols for Satellite Ocean Color Sensor Validation, Revision 4, Volume III: Radiometric Measurements and Data Analysis Protocols*, NASA/TM-2003-21621/Rev-Vol. III, 21–31.
32. Qi, L., C. Hu, Q. Xing, and S. Shang (2016). Long-term trend of *Ulva prolifera* blooms in the western Yellow Sea. *Harmful Algae*, *58*:35-44. <http://dx.doi.org/10.1016/j.hal.2016.07.004>
33. Qi, L., C. Hu, M. Wang, S. Shang, and C. Wilson (2017). Floating algae blooms in the East China Sea. *Geophysical Research Letters*, *44*. <https://doi.org/10.1002/2017GL075525>.
34. Qi, L., C. Hu, P. M. Visser, and R. Ma (2018). Diurnal changes of cyanobacteria blooms in Taihu Lake as derived from GOCI observations. *Limnol. Oceanogr.*, *63*:1711-1726. doi: 10.1002/lno.10802.
35. Qi, L., Hu, C., Mikelsons, K., Wang, M., Lance, V., Sun, S., Barnes, B. B., Zhao, J., & Van der Zande, D. (2020). In search of floating algae and other organisms in global oceans and lakes. *Remote Sensing of Environment*, *239*, 111659. <https://doi.org/https://doi.org/10.1016/j.rse.2020.111659>
36. Qi, L., and C. Hu (2021). To what extent can *Ulva* and *Sargassum* be detected and separated in satellite imagery? *Harmful Algae*, *103*, 102001, <https://doi.org/10.1016/j.hal.2021.102001>

37. Roberts, A.J., & Conover, M.R. (2013). Eared grebe diet on Great Salt Lake, Utah, and competition with the commercial harvest of brine shrimp cysts. *The Journal of wildlife management*, *77*, 1380-1385
38. Rouse, J. W., Haas, R. H., Schell, J. A., & Deering, D. W. (1974). Monitoring vegetation systems in the Great Plains with ERTS. *NASA special publication*, *351*(1974), 309-317.
39. Shamsolmoali, P., Zareapoor, M., Wang, R., Zhou, H., & Yang, J. (2019). A novel deep structure u-net for sea-land segmentation in remote sensing images. *IEEE Journal of Selected Topics in Applied Earth Observations and Remote Sensing*, *12*(9), 3219-3232.
40. Stephens, D.W., & Gillespie, D.M. (1976). Phytoplankton production in the Great Salt Lake, Utah, and a laboratory study of algal response to enrichment1. *Limnology and Oceanography*, *21*, 74-87.
41. Sura, S.A., & Belovsky, G.E. (2016). Impacts of harvesting on brine shrimp (*Artemia franciscana*) in Great Salt Lake, Utah, USA. *Ecological Applications*, *26*, 407-414.
42. Van Stappen, G. (1996). Introduction, biology and ecology of *Artemia*. In P. Lavens & P. Sorgeloos (Eds.), *Manual on the production and use of live food for aquaculture* (Vol. 361, pp. 79–106). Rome, Italy: FAO.
43. Vanhaecke, P., Tackaert, W., & Sorgeloos, P. (1987). The biogeography of *Artemia*: an updated review. *Artemia research and its applications*, *1*, 129-155.
44. Wurtsbaugh, W.A., & Maciej Gliwicz, Z. (2001). Limnological control of brine shrimp population dynamics and cyst production in the Great Salt Lake, Utah. *Hydrobiologia*, *466*, 119-132.
45. Wurtsbaugh, W.A., Miller, C., Null, S.E., DeRose, R.J., Wilcock, P., Hahnenberger, M., Howe, F., & Moore, J. (2017). Decline of the world's saline lakes. *Nature Geoscience*, *10*, 816-821.
46. Xiao, X., Lian, S., Luo, Z., & Li, S. (2018, 19-21 Oct. 2018). Weighted Res-UNet for High-Quality Retina Vessel Segmentation. 2018 9th International Conference on Information Technology in Medicine and Education (ITME), 2018, pp. 327-331, doi: 10.1109/ITME.2018.00080.
47. Yamano, H., Sakuma, A., & Harii, S. (2020). Coral-spawn slicks: Reflectance spectra and detection using optical satellite data. *Remote Sensing of Environment*, *251*, 112058. <https://doi.org/https://doi.org/10.1016/j.rse.2020.112058>
48. Zhang, Z., Liu, Q., & Wang, Y. (2018). Road Extraction by Deep Residual U-Net. *IEEE Geoscience and Remote Sensing Letters*, *15*(5), 749-753. <https://doi.org/10.1109/LGRS.2018.2802944>

Tables and captions

Table 1. Spectral Angle Mapper (SAM, °) index between the BSC reference spectrum (maximum spectrum in Fig. 1b) and reflectance spectra of various floating materials (including BSC) for OLCI wavelengths of 510, 560, 620, 681, 709, 754, and 865 nm. Note that SAM for BSC (bold font) is significantly lower than for other floating materials except coral spawn eggs, indicating unique spectral shapes in BSC reflectance.

Floating matter	BSC (lab) ^a	BSC (field) ^b	BSC (OLCI) ^c	BSC (OLCI) ^d	Non-BSC (OLCI) ^e	Plastics (lab)	Pumice (OLCI)	Cyano-bacteria	Whitecaps (field)	Coral spawn (field)
SAM (°)	3.3±2.7	5.1±0.6	8.4±1.9	5.6±2.0	23.4±2.8	25.5±3.8	22.6±2.2	26.4±1.4	42.4±2.2	13.5±3.2
Ref	Fig. 1b	Fig. 2c	Fig. 2d	Qi et al.	Fig. 4b	Hu (2021)	Qi et al.	Qi et al.	Dierssen (2019)	Yamano et al

^aLaboratory-measured BSC spectra (Fig. 1b) other than the reference spectrum

^bField-measured BSC spectra after subtracting water background (Fig. 2c and Fig. 2d dashed lines)

^cOLCI-derived BSC spectra after subtracting water background (Fig. 2d solid lines)

^dOLCI-derived BSC spectra after subtracting water background (Fig. 11c of Qi et al., 2020)

^eOLCI-derived non-BSC spectra after subtracting water background (Fig. 4b)

Figure captions

Fig. 1. Reflectance measurements of BSC samples floating on saline water. (a) Experimental setting (not drawn on scale), with photo examples of commercial BSC covering different proportions of saline water surfaces in small, transparent containers. The small container is put in a larger, black container filled with salt water to take reflectance measurement. (b) Sample reflectance (dimensionless) of varying amounts of surface coverage, such as those shown in (a). Also plotted is the reflectance from a pixel of OLCI image over the GSL on 9 June 2019 (same as in Fig. 11c of Qi et al., 2020), where reflectance difference is shown in the second y-axis. The two arrows indicate the inflections in the reflectance spectra at ~ 550 nm and ~ 650 nm, respectively. (c) Reflectance at 754 nm (relative to background water) versus dry BSC biomass per surface area.

Fig. 2. (a) Digital photos collected from the GSL on 17 Dec 2019 (approximately 40.78°N 112.24°W , annotated with a red “+” in Fig. 4a) showing surface BSC slicks with varying amounts of surface coverage. (b) *In situ* reflectance spectra (R , dimensionless) corresponding to the photos. The two arrows indicate the inflections in the reflectance spectra at ~ 550 nm and ~ 650 nm, respectively; (c) Reflectance difference (ΔR) between the cyst slicks and lake water; (d) The same ΔR plotted in log scale. Overlaid are the OLCI ΔR_{rc} spectra of Fig. 4e (solid lines with filled circles, p1 – p3). The spectral shapes are nearly identical (i.e., parallel to each other in log space) regardless of their magnitudes, as explained by Eq. 9.

Fig. 3. Flowchart showing the technical steps of (1) Step 1: preparation of training and validation images, (2) Step 2: training and validation of the ResUNet deep learning model, and (3) Step 3: application of the DL model to derive time-series of gridded BSC maps. Further details are presented in the main text.

Fig. 4. (a) Sentinel-3B/OLCI FGRB image over the GSL (location annotated in the inset map) showing image slicks in both the north arm and south arm, but due to different floating matters on the surface. (b) & (c) OLCI ΔR_{rc} spectra from image slicks in the north arm, plotted in linear

scale and log scale, respectively. (d) & (e) OLCI ΔR_{rc} spectra from image slicks in the south arm, plotted in linear scale and log scale, respectively. The slicks in the south arm are confirmed to be BSC aggregations according to their spectral shapes as compared with those obtained from laboratory and *in situ* measurements (Figs. 1&2). The colored circles/squares in (a) show the locations corresponding to the spectra in (b) – (e). Red “+” in (a) shows the location of *in situ* measurement of Fig. 2.

Fig. 5. MERIS (top row) and OLCI (bottom row) examples showing extraction of BSC slicks using the DL model. (a) and (b): FRGB images showing BSC slicks and other features (e.g., clouds in red circles); (c) and (d): same images but with DL extraction results overlaid and areal density (χ from 0% to 5%) color coded. The color code applies to the slicks only; (e) and (f): NDVI images showing the difficulty in separating clouds (red circles) from BSC slicks when being used alone; (g) and (h): typical ΔR_{rc} spectra from BSC slicks (locations annotated in (a) and (b) with colored circles). Full-size images corresponding to (a) – (d) are presented in Fig. S1 of the supplemental materials.

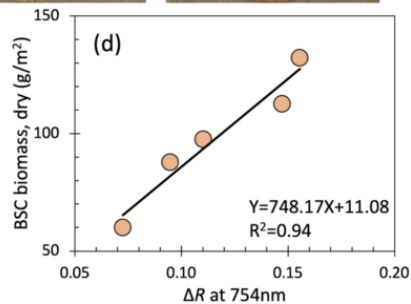
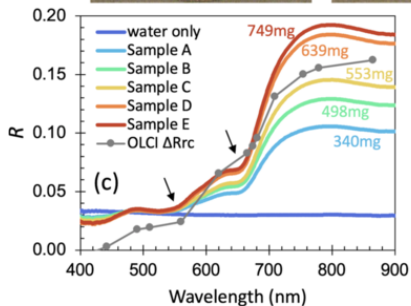
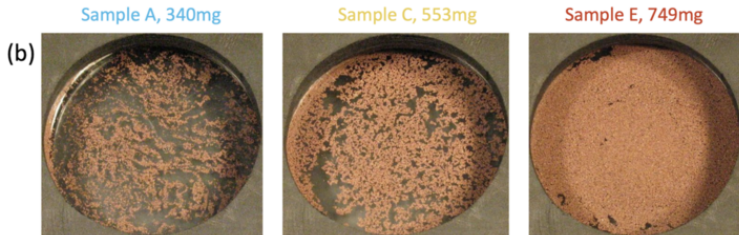
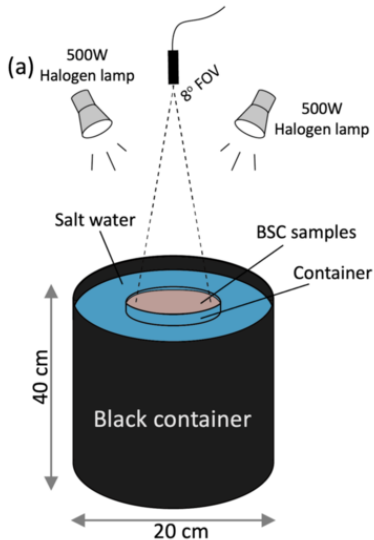
Fig. 6. (a) Monthly mean BSC abundance, represented by the BSC surface coverage (in km²), from MERIS (2002/05 – 2012/04, orange bars) and OLCI (2016/04 – 2020/08, blue bars), respectively. (b) Climatology monthly mean abundance of BSC from combined MERIS and OLCI. (c) Annual mean abundance of BSC from MERIS (orange bars) and OLCI (blue bars), and the annual BSC harvest biomass (gray squares in kilo tons) from 2002 to 2020. All data refer to the south arm of the GSL.

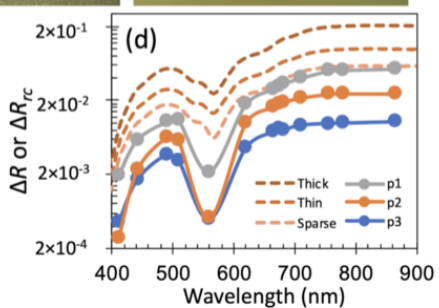
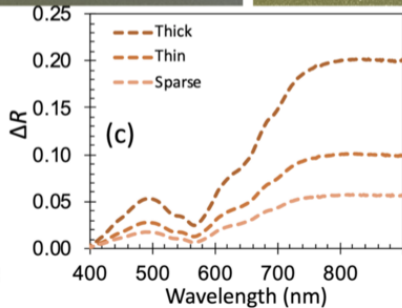
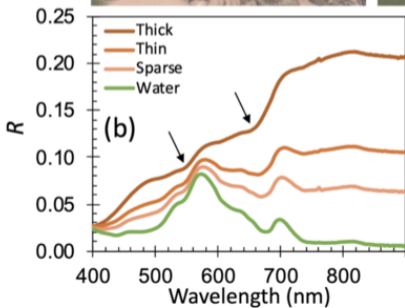
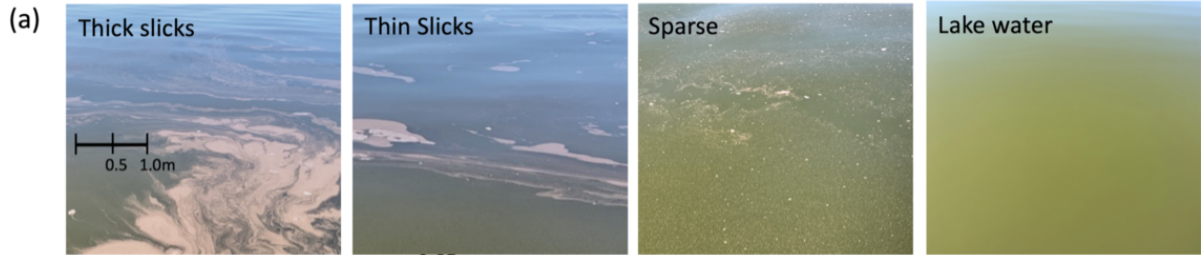
Fig. 7. (a) Distribution of BSC areal density (in % cover) in each climatological month from MERIS (2002 - 2012) and OLCI (2016 - 2020) for the south arm of the GSL; (b) Number of valid pixels (after masking clouds) in each grid in each climatological month.

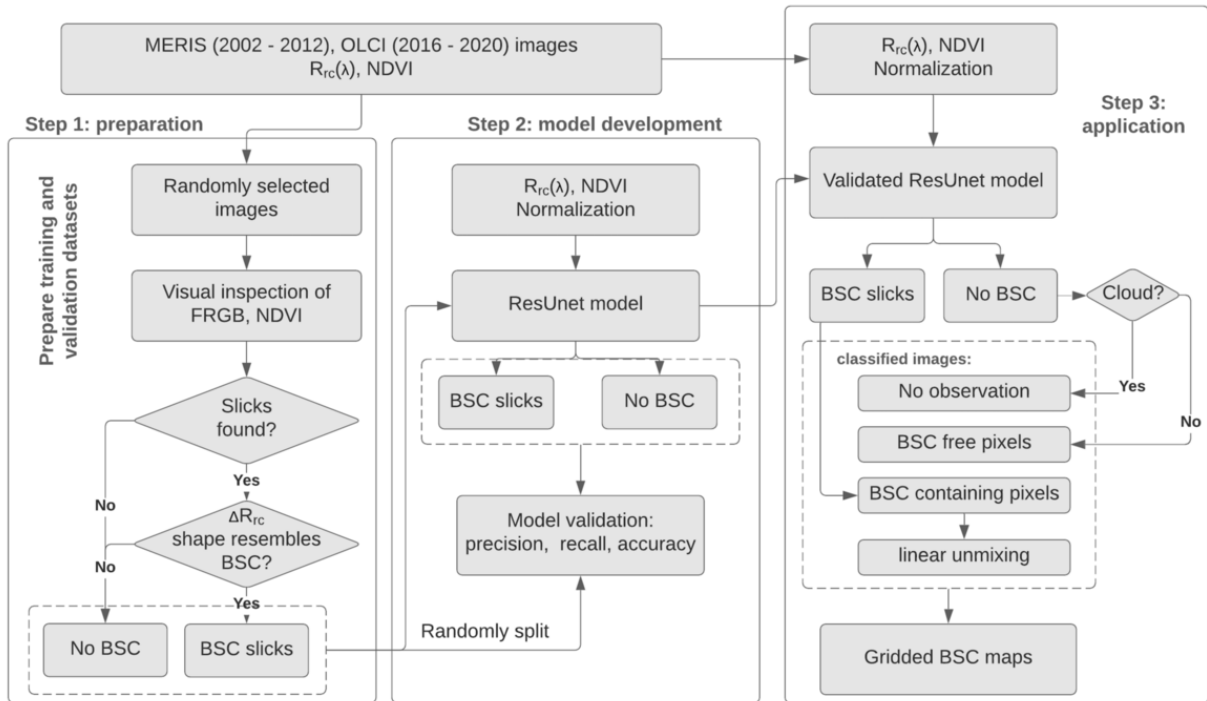
Fig. 8. (a) Rose diagram showing statistics of wind direction and wind speed over the GSL, with the latter color coded for 0 – 8 m/s. (b) and (c): climatology monthly and annual mean air

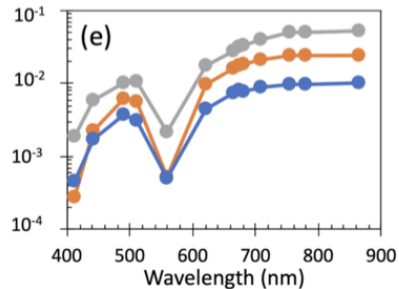
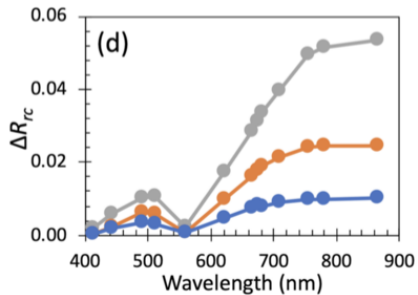
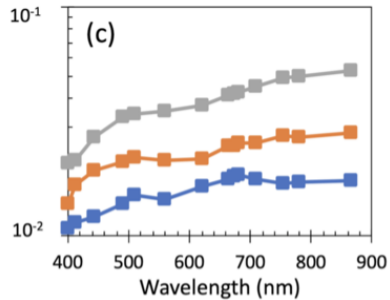
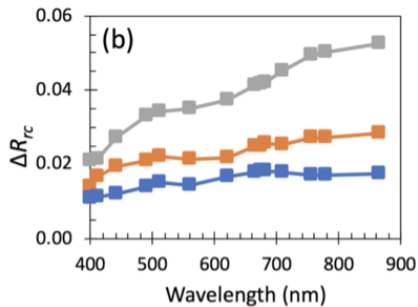
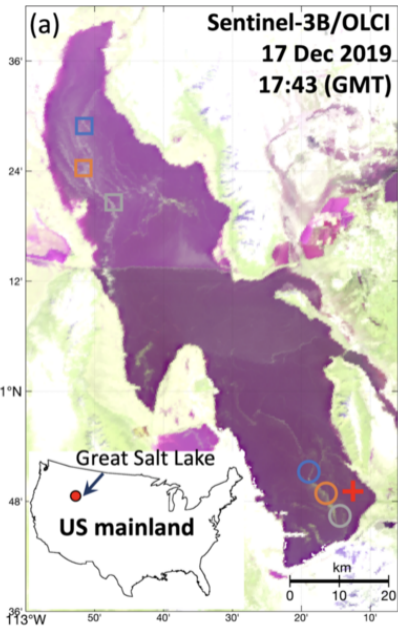
temperature, wind speed, and salinity, respectively. Here, salinity refers to the south arm of the GSL.

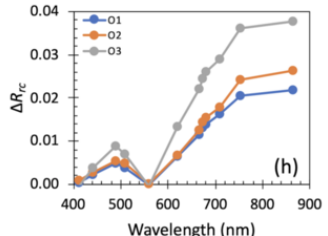
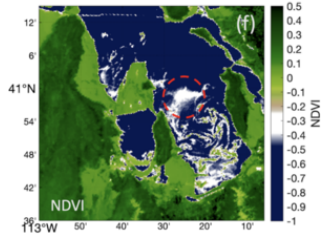
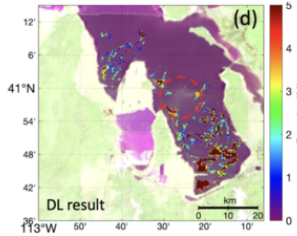
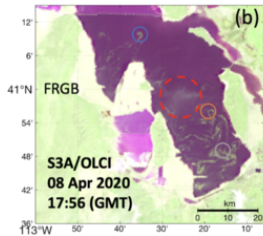
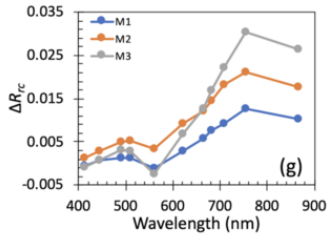
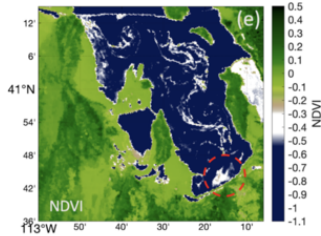
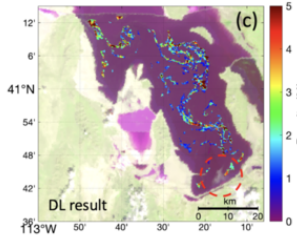
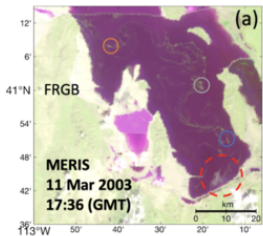
Fig. 9. BSC slicks and corresponding typical spectra from several other salt lakes. (a) South Aral Sea; (b) Lake Urmia; (c) Dead Sea. The corresponding typical OLCI spectra from the BSC slicks are shown in (d) – (f), respectively, with locations and spectral symbols color coded in the same way.

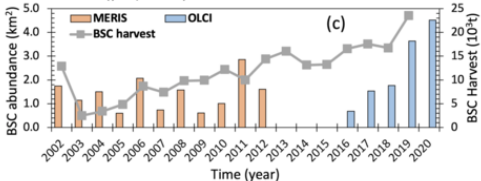
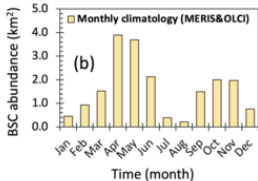
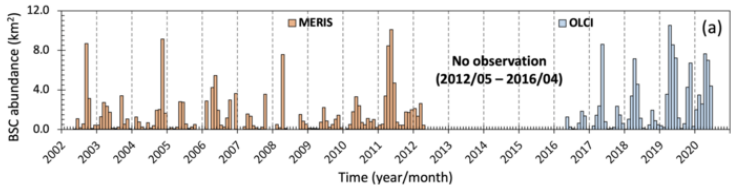


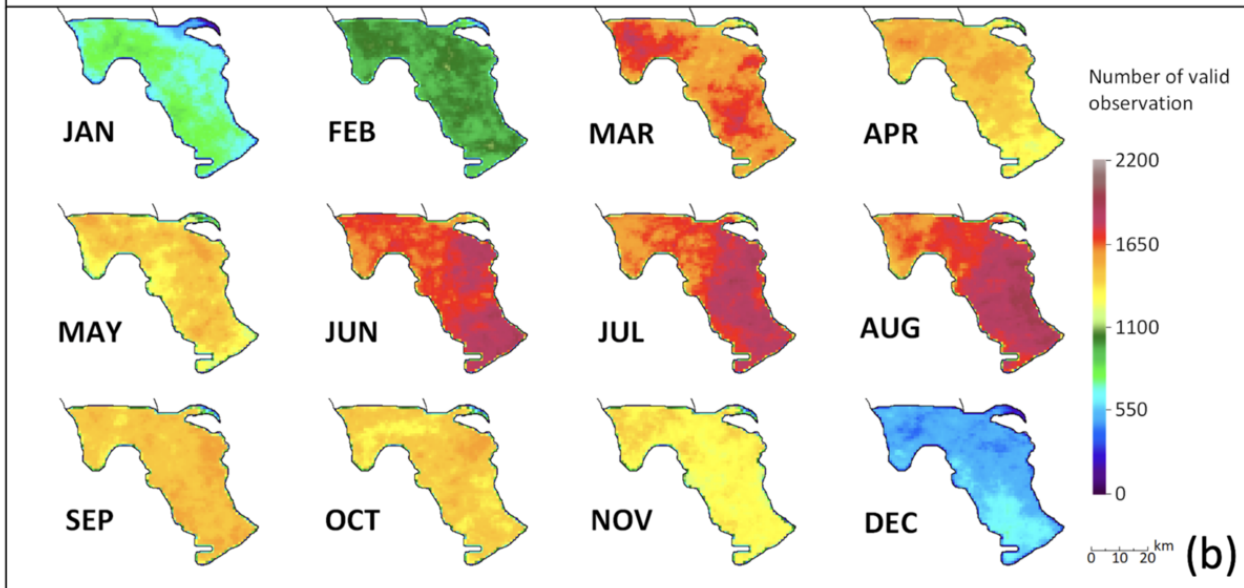
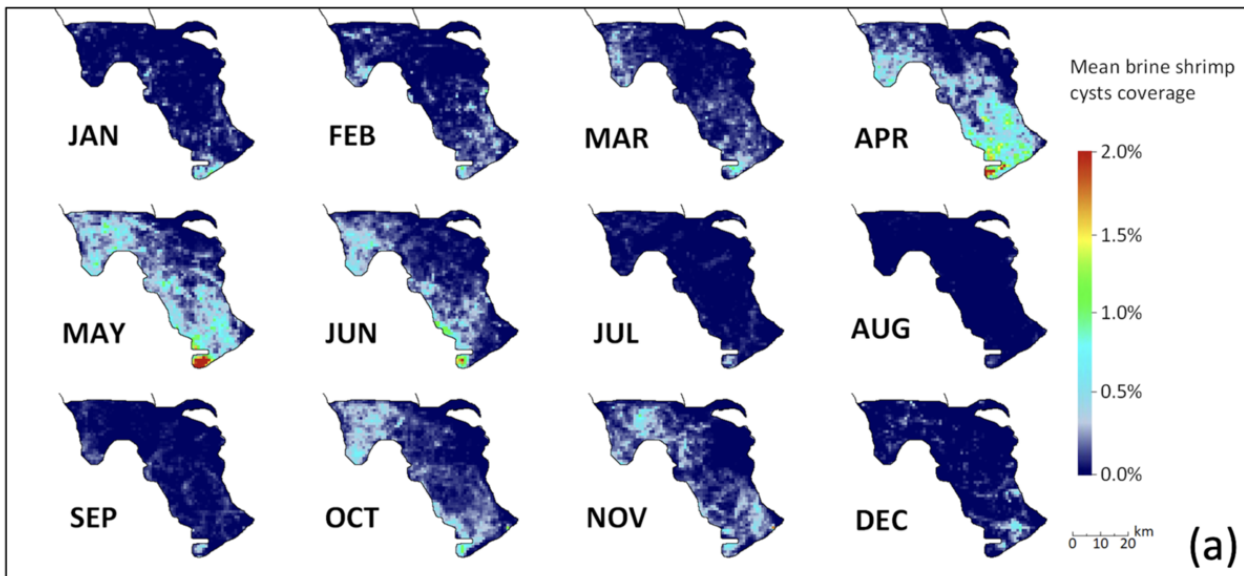


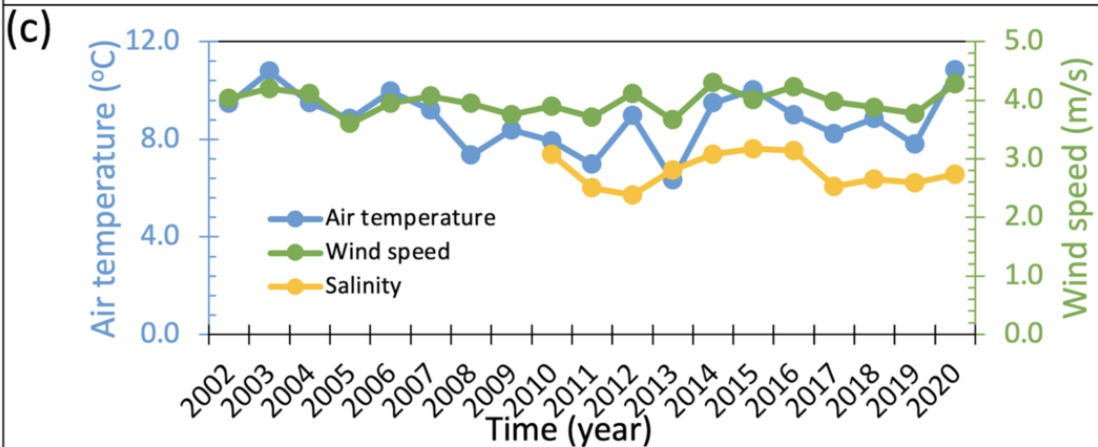
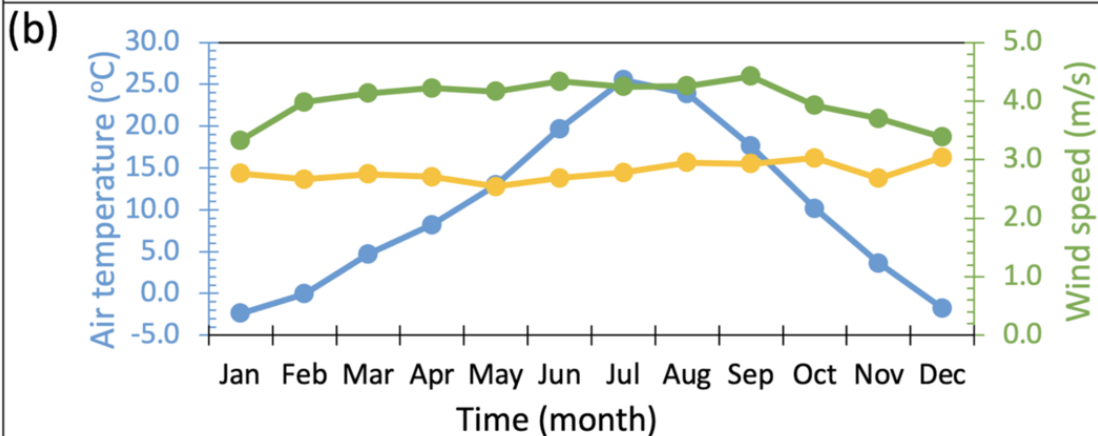
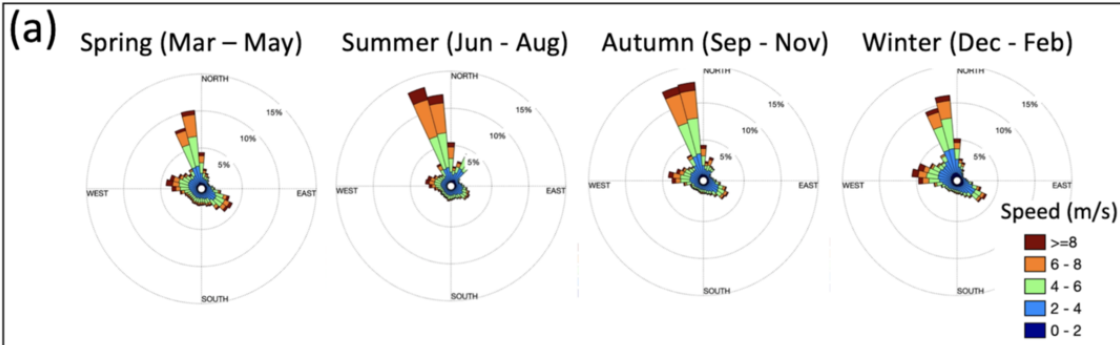


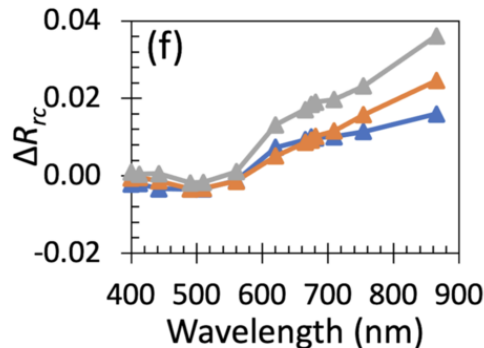
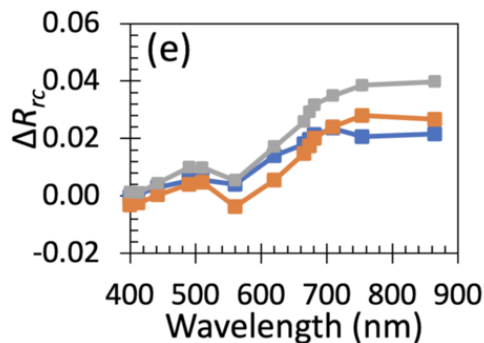
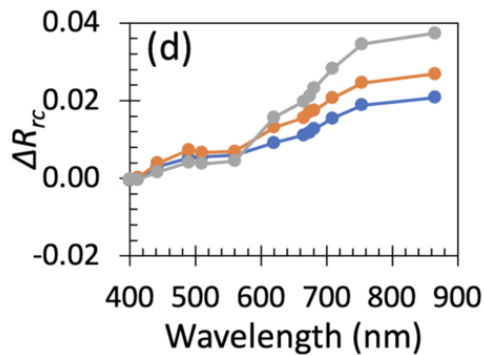
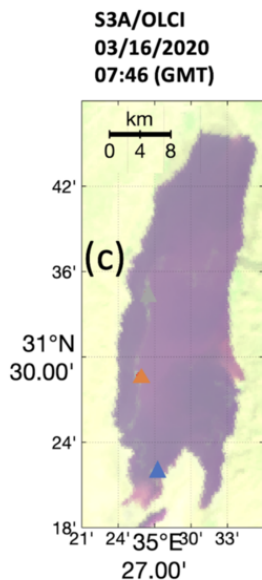
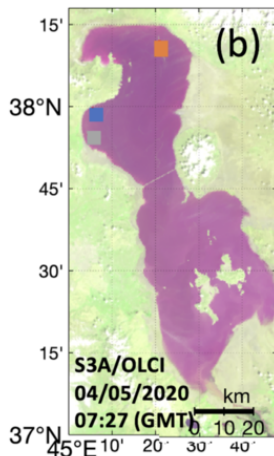
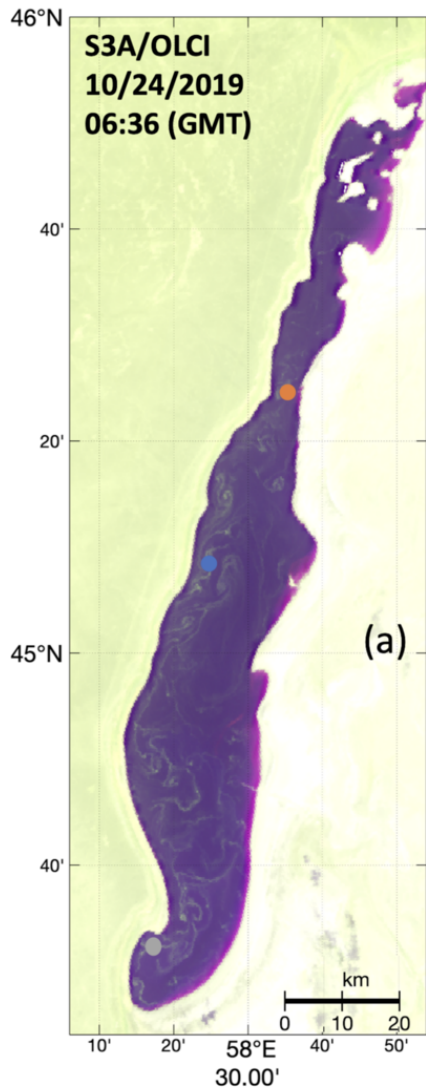












Graphical Abstract

Surface aggregations of brine shrimp (*Artemia*) cysts (BSC) in salt lakes show unique reflectance spectral shapes, therefore can be identified from passive optical remote sensing imagery. Based on the spectral and spatial characteristics of surface aggregations of BSC, a deep learning model is developed to detect and quantify surface BSC in the southern arm of the Great Salt Lake from satellite imagery of 2002 – 2012 and 2016 – 2020. Results show clear seasonality, inter-annual variability, and a recent increase in BSC amount. While such information may complement those obtained from shipborne surveys to help understand the lake's ecology and fisheries, the study represents the first of its kind in satellite remote sensing of shrimp eggs, which may be extended to other salt lakes on Earth to have a systematic evaluation.

